Chapter 8
Comparisons of CFD Calculations and Measurements for a Sonic Methane Plasma Jet in a Supersonic Crossflow

"The outcome of any serious research can only be to make two questions grow where only one grew before." Thorstein Veblen

Extensive testing with a plasma torch operating on methane in a supersonic crossflow sparked an interest in modeling the torch using CFD to determine if methane plasma jets can be accurately modeled, and if so, to ascertain the usefulness of such results. The comparison presented here is of a methane plasma jet produced by a normally oriented plasma torch in a Mach 2.4 crossflow and the corresponding CFD model. Total temperature probing and computational calculations for a plane at 49.6 diameters downstream of the torch were the basis for comparison. In addition, shadowgraphs were compared to calculated density variations near the torch exit. CFD plots of several major species are presented as well to provide an understanding of where combustion is expected to occur in the flowfield.

CFD calculations were made using GASP® (General Aerodynamic Simulation Program). Analysis of the probing and calculations shows that the CFD predicts the penetration height and shape of the centerline profile well; although there are noted areas of needed improvement to make the CFD calculations match the experimental results more closely. In addition, the CFD produced a shock profile with a bow shock angle only 2° higher than the 30° angle observed in experiments.

8.1: Experimental Conditions

The plasma torch modeled was VTPT-3, with an anode constrictor length of 2.54 mm and an exit diameter of 1.59 mm. In addition, the constrictor exhausted directly into the crossflow (i.e. no diverging section). The plasma torch chamber pressure was 446 kPa and the input power was 1500 W. Sonic conditions were assumed at the torch exit, both because of the pressure differential between the torch and tunnel, and arc heating within the constrictor. The freestream Mach number was 2.4, with a total temperature of approximately 280 K. Earlier experimental measurements evaluated the boundary layer thickness under these conditions to be 1 cm.

8.2: Computational Methodology

The CFD calculations were performed using GASP®, a finite-volume, high-speed flow CFD program developed by the Aerosoft Company. Personnel of Aerosoft also performed the present CFD calculations (Viti, 2000). GASP® solves the integral form of the time-dependent Reynolds-averaged Navier-Stokes (RANS) equations in three dimensions using a structured grid design. Finite rate reacting flows can be implemented as well. The physical modeling capabilities of GASP® are enhanced by the choice of four thermodynamic models, and supports twenty different chemistry models. The thermochemistry includes real gas mixtures, both calorically and thermally imperfect, and finite rate chemistry. For this case, a simple methane-air reaction mechanism was implemented.

A converged solution was defined for a maximum residual of three orders of magnitude. In addition, the flowfield data at 49.6 diameters downstream were checked to see if any significant changes in the flowfield properties were occurring compared to earlier time-step solutions. The maximum total temperature was found to change less than 0.1 K for the final solution, compared to the previous time-step.

8.2.1: Jet and Boundary Conditions

The plasma jet exit parameters were simulated using extrapolations of experimental data and assumptions about the exit temperature profile, velocity, and density. The mass flow rate of methane through the torch was calculated to be 0.17 g/s, found by using the torch chamber pressure and known choking area. To model a torch operating at 1500 W, it was assumed that approximately 40% of the energy entered the gas, where the remaining 60% was assumed to be lost to the electrodes through joule heating or radiation to the surroundings. Typical values for plasma torch efficiencies of this design range from 40 to 60%. Absorbing 600 W with a flowrate of 0.17 g/s, the bulk temperature of the methane exiting the torch was calculated to be 1080 K. From this a temperature profile was assumed, in which the maximum centerline temperature was 6000 K, the wall temperature was 400 K, and the temperature gradients at these two boundaries were zero. The centerline temperature of 6000 K was based on a blackbody curve fit to spectral data of methane, which predicted an effective blackbody temperature

of just under 6000 K for the methane plasma jet. The equation used to produce this profile is

$$T = 5605 \cdot \exp(-272 \cdot x) + 398.7 \tag{8.1}$$

where x is the radius at which the temperature is to be calculated (0 to 0.03125-in.). This equation produces a sharp temperature profile near the centerline, characteristic of plasmas where only a small fraction of the gas exceeds 3000 K. From these assumptions, the total pressure at the throat exit was calculated to be 96.3 kPa. The velocity profile was assumed to be uniform.

The computational volume surrounding the jet was defined as shown in Figure 8.1. The volume extended 2.54 cm upstream of the jet exit, 7.91 cm downstream, 2.54 cm cross-stream, and 5.08 cm above the jet exit. Freestream conditions were modeled such that the Mach number was 2.4, the total temperature was 298 K, and the total pressure was 379.1 kPa. With the plasma torch operating at chamber pressure of 446 kPa, this produced a jet-to-tunnel momentum flux ratio of 1.17. The boundary layer from the experimental work is approximately 1 cm thick, and was modeled as a standard turbulent boundary layer at the flow entrance to the computational domain. The tunnel floor was modeled as a no-slip, adiabatic wall. Free surfaces were modeled using an extrapolation scheme, such that fluid could leave the computational domain.

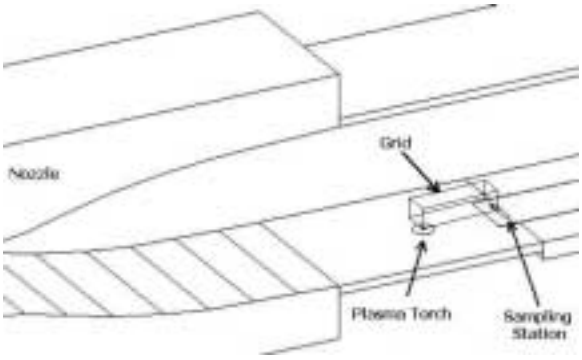

Figure 8.1: Illustration of Computational Grid Location

8.2.2: Grid Generation

The grid generation code for this analysis was GRIDGEN®. GRIDGEN® is a graphical, interactive grid-generating program used for producing three-dimensional grids for CFD solvers such as GASP®. Grid points are defined through various routines,

such as hyperbolic or geometric progression, to achieve a desired grid distribution. The volume of the grid is comprised of blocks, which together form the computational domain. Blocks are designed so that grid point density is increased in areas requiring high resolution and decreased where resolution is not as important, such as far out into the freestream.

A CFD solver such as GASP® can use the output blocks produced by the GRIDGEN® code. For this case, seventeen blocks were used to define the computational domain, and grid sequencing was implemented to speed up convergence. Clearly, the most important volume to be modeled is the volume surrounding the plasma jet exit, and therefore was given special attention. An H-type grid was used for the jet exit, with the symmetry plane lying along the centerline of the jet and parallel to the direction of the crossflow. H-type grids increase resolution over radial or rectangular grids and do not create a singularity point at the center of the jet. Directly encompassing the jet exit area was a C-type grid. This area, consisting of the H and C-type grids, was then extruded along a path the jet plume was expected to follow. Surrounding blocks were designed to compliment these grids, using a geometric progression for defining the grid points along the block boundaries. This provided extra detail near the jet exit where it was needed most. In total, seventeen blocks were used to define the computational domain, consisting of 154,800 grid points. An isometric view of the computational domain is shown in Figure 8.2.

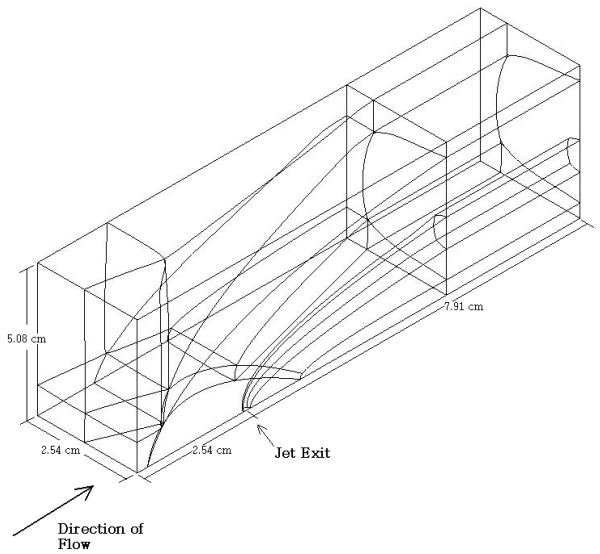

Figure 8.2: The Computational Domain and Block Structure

8.2.3: Reaction Mechanism

The reaction mechanism used to model the methane combustion was developed by Bowman and Seery (1972) and is shown below in Table 8.1. The mechanism consists of 13 species and 11 reactions, and was developed for methane oxidation in air. Some key aspects of the mechanism are that it contains a basic H_2-air mechanism, which is crucial. Furthermore, CO oxidation is controlled by the hydroxyl radial (OH) and the methyl radial (CH_3) dominates during the initial phase of the oxidation process. However, it is noted that this model does not contain charged species to accurately represent the kinetics associated with the plasma jet, nor does it contain some of the chain-branching and chain-terminating reactions. This mechanism was coded into GASP® to model the combustion of methane. The reaction scheme was adopted as a compromise between modeling reality and computation efficiency for a 3D, Navier-Stokes calculation.

Table 8.1: Bowman and Seery Reaction Mechanism for Methane

$k_f = AT^b exp(-E/RT)$

	Reaction	Forward		
		A	b	E/R
1.	$CH_4+M=CH_3+H+M$	2×10^{17}	0	44.5×10^3
2.	$CH_4+OH=CH_3+H_2O$	2.8×10^{13}	0	2.5×10^3
3.	$CH_4+O=CH_3+OH$	2×10^{13}	0	4.64×10^3
4.	$CH_4+H=CH_3+H_2$	6.9×10^{13}	0	5.95×10^3
5.	$CH_3+O_2=H_2O+CHO$	2×10^{10}	0	0
6.	$CH_3+O=CHO+H_2$	1×10^{14}	0	0
7.	$CHO+OH=CO+H_2O$	1×10^{14}	0	0
8.	$CHO+M=H+CO+M$	2×10^{12}	½	14.4×10^3
9.	$O+N_2=NO+N$	1.4×10^{14}	0	3.79×10^3
10.	$N+O_2=NO+O$	6.4×10^9	1	3.14×10^3
11.	$N+OH=NO+H$	4×10^{13}	0	0

$$[A] \rightarrow \frac{cm^3}{gmol \cdot s}$$

8.3: Results and Discussion

Three comparisons were made between the results obtained from the CFD calculations and the experimental results: downstream 2D temperature profiles at 49.8 diameters, a centerline temperature profile at the same distance, and the shock structure near the jet. The two centerline profiles are shown in Figure 8.3. Two distinct features are instantly recognized. First, the maximum total temperature ratio predicted using GASP® is about 8% lower than the experimental results. Second, the shapes of the two

profiles look much the same, except that the profile produced with GASP® has a consistently lower total temperature ratio. The vertical distance of the total temperature ratio maxima, defined as the penetration height, are both located 3.25 diameters above the tunnel floor. In addition, the shape of the profiles below the maxima both appear to exhibit similar trends, except that the temperature of the CFD profile approaches that of the freestream, indicating that no thermal energy has been trapped in the shear layer. However, above the maxima, the profile produced by the CFD has a steeper gradient. These trends indicate that the CFD predicts the penetration height of the plume rather well, but does not accurately account for the distribution of thermal energy about this maximum. The possible sources for these differences will be discussed later.

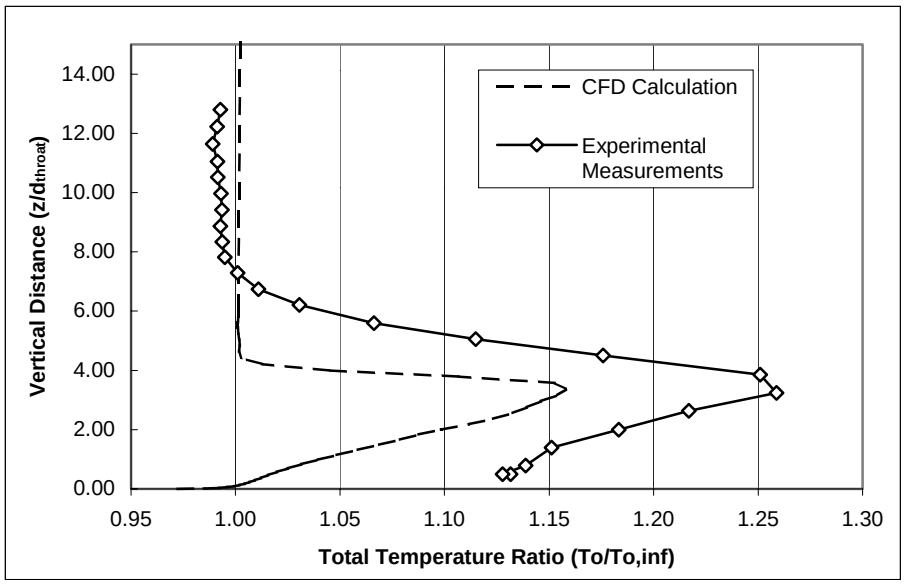

Figure 8.3: Centerline Total Temperature Profile Comparison for 1500 W

The 2D total temperature profiles are shown in Figure 8.4, where they are presented on the same physical scale. Here, there are marked differences in the shape of the profiles, more so than with the centerline profiles. Although the cores are both at relatively the same height, the experimental results exhibit a much larger core. In addition, the experimental results show that hot gases are present along the floor of the tunnel trapped in the shear layer, whereas with the CFD results, full penetration of the thermal energy is attained. This immediately indicates a problem with the ability of the

Baldwin-Lomax turbulence model to accurately represent the thermo-fluid mechanics in the shear layer. Methods to overcome this problem will be discussed in Section 8.3.1.

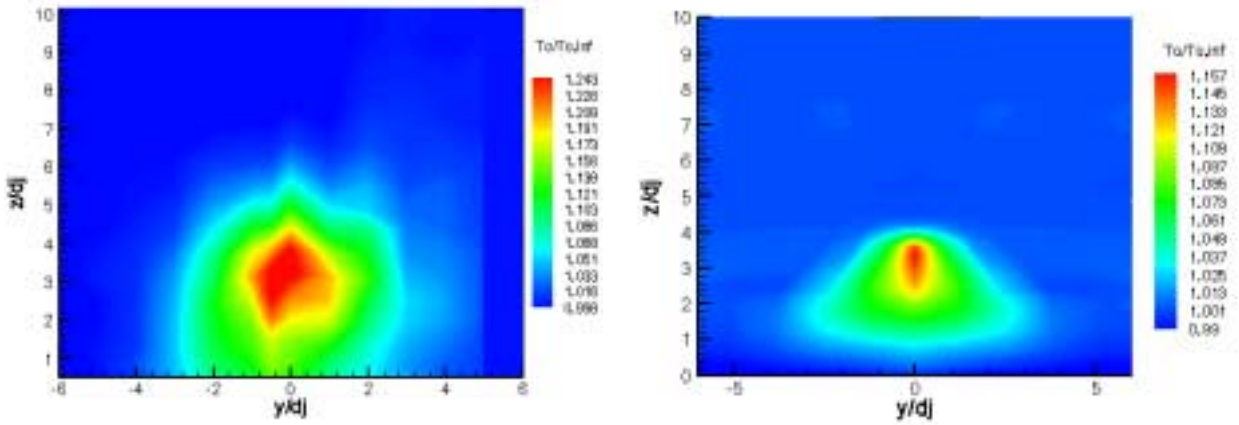

(a) Experimental Results (b) CFD Results

Figure 8.4: Complete Total Temperature Profile Comparison for 1500 W

The comparison between the experimental shadowgraph and density variations from the CFD calculations is shown in Figure 8.5. In both figures, the flow is from left to right, and the bow shock angle is defined as the angle the bow shock makes between the edge of the boundary layer and the edge of the frame (illustrated in Figure 7.16). The CFD results are presented on the left and show density variations in the flow. The blue areas identify the plume, while the shock is just upstream of the red area. The boundary layer edge is located at the point of transition from yellow to orange. In this figure the shape of the bow shock can be clearly seen and measured. The shadowgraph shows a similar shock structure, and although grainy, is still easily identified. The CFD calculations resulted in a bow shock angle of 32°, and for the corresponding experimental work, 30°.

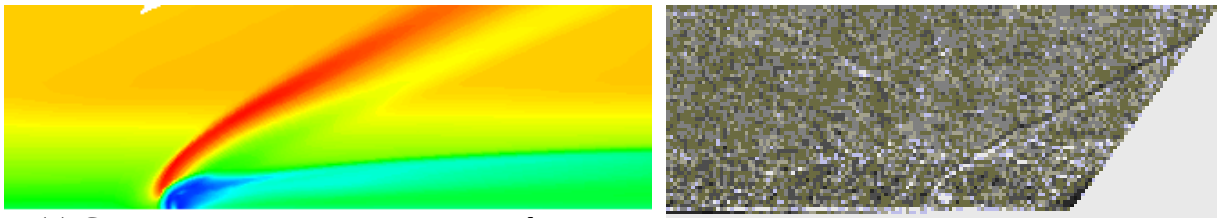

(a) CFD Density Variations Near Torch Exit (b) Shadowgraph

Figure 8.5: Shock Structure Comparison for 1500 W and a q_t of 1.18

Predicted mass fraction plots are shown in Figure 8.6 for H, H_2, H_2O, and OH. The maxima and minima mass fractions for each specie are tabulated in Table 8.2, where the minima, rather than being presented as zero, are defined as the mass fraction at the edge of the identifiable plume for each specie. Also, a white arrow indicates the torch exit for those plots where it is not apparent. As with Figure 8.5, the plots here show flow from left to right, with the plasma torch exit upstream of bottom-center. From Figure 8.6a it is clear that hydrogen atoms exist for a very short period of time. H_2 molecules, shown in Figure 8.6b, appear to penetrate to what can loosely be defined as the edge of the plasma jet. Both of these trends are consistent with the experimental spectrographic results presented in Chapter 6. OH molecules in Figure 8.6c are characteristic of regions where intense combustion occurs. From these results, the most intense areas of combustion should occur at about 2.5 cm downstream of the torch and 0.8 to 1.0 cm off of the floor. Finally, the presence of H_2O molecules in Figure 8.6d is indicative of complete combustion.

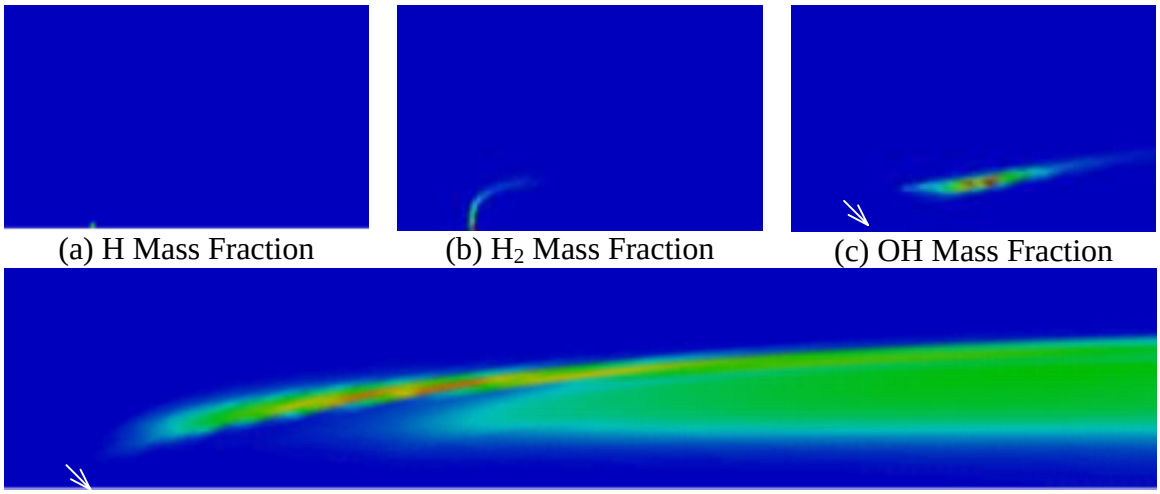

(a) H Mass Fraction (b) H_2 Mass Fraction (c) OH Mass Fraction

(d) H_2O Mass Fraction (10.7 cm x 2.0 cm)

Figure 8.6: CFD-Predicted Mass Fractions of Some Major Species
(scale for a, b and c: 3.3 cm x 2.0 cm)

Table 8.2: Mass Fraction Maxima and Minima

Specie	Maxima	Minima
H	5.67×10^{-4}	9.63×10^{-13}
H_2	2.46×10^{-3}	5.54×10^{-13}
OH	2.03×10^{-16}	4.05×10^{-17}
H_2O	1.99×10^{-5}	3.98×10^{-6}

In addition to the plots of mass fraction values near the torch exit, mass fraction profiles at 49.6 d_{eq} were constructed and are presented in Figure 8.7 and 8.8. Figure 8.7 shows mass fraction profiles for hydrocarbon fragments and molecules produced from combustion reactions, while Figure 8.8 shows mass fraction profiles for N_2 and O_2. Table 8.3 lists the maximum mass fraction values for each of the species. All species not listed in this table (i.e. CO, H, N, NO and O) had mass fractions below $1x10^{-10}$ and were considered insignificant. The exception is OH, with a maximum mass fraction of $4.32x10^{-20}$, but is shown here because of its chemical importance to the combustion process and the interesting plume structure it exhibits.

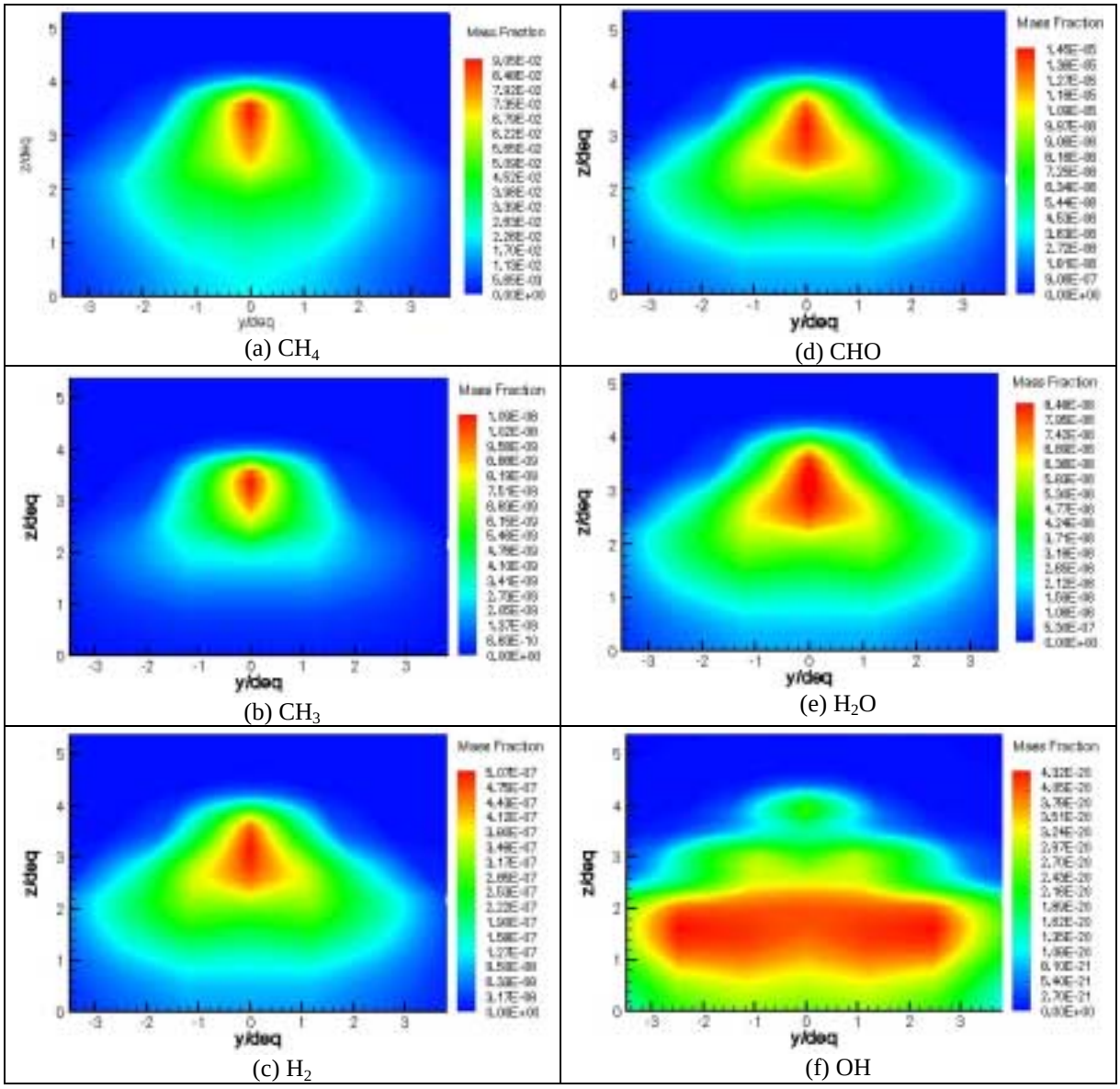

(a) CH_4 (d) CHO

(b) CH_3 (e) H_2O

(c) H_2 (f) OH

Figure 8.7: CFD-Predicted Mass Fraction Plots at 49.6 d_{eq} Downstream of Torch Exit

There are several identifiable trends produced by the CFD calculations. First, except for OH, all the hydrocarbon species have their maximum mass fraction at the same location as the maximum total temperature ratio and exhibit similar plume shapes to the total temperature plot shown in Figure 8.4. Also, some species exhibit more spreading, or mixing, such as H_2, H_2O and CHO. The presence of CH_4 shows that there is incomplete burning of the methane feedstock by the torch. Comparison of the concentrations of CH_4 and H_2O shows a difference of four orders of magnitude, indicating that only a minute portion of the methane feedstock has undergone complete combustion. This agrees quite well with the experimental results presented in Chapter 7, although the amount of combustion realized experimentally is probably somewhat larger than predicted by CFD. The presence of CHO is an indicator that the flame is chilled, which is certainly the case in an unheated supersonic environment (Gaydon, 1974). CH_3, present in low-pressure methane flames, appears to be concentrated mainly near the plume core with very little lateral or vertical variation. The existence of OH at this location indicates that a very small portion of the flow is still reactive. The plume shape of OH, although quite different than the other molecules presented, can probably be attributed to the low concentration and rate of diffusion of the OH molecule.

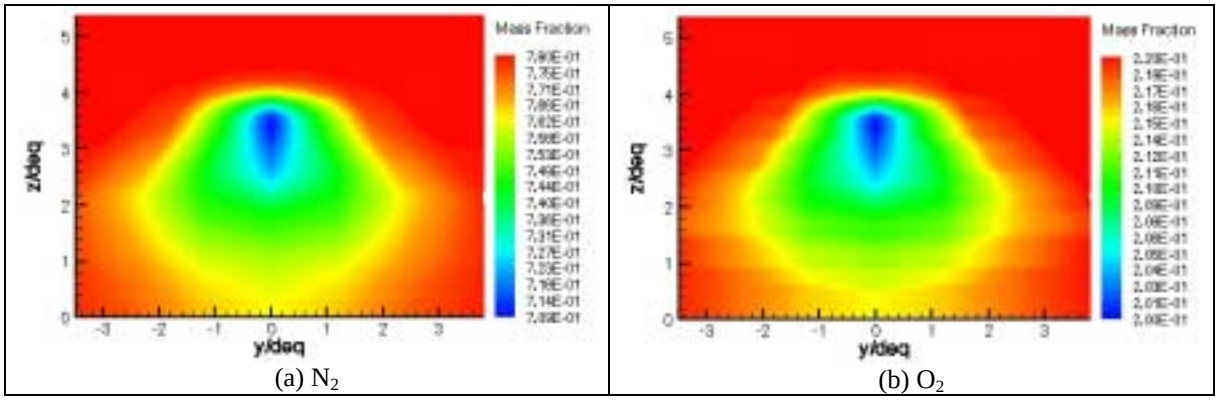

(a) N_2 (b) O_2

Figure 8.8: CFD-Predicted Air Mass Fraction Plots at 49.6 d_{eq} Downstream of Torch Exit

The two plots for N_2 and O_2 are shown in Figure 8.8. Expectedly, the maxima concentrations for these molecules occur away from the plume, out in the freestream, and the minima occur in what was previously identified as the plume core. This trend demonstrates that some of the available oxygen has been used in combustion to produce

H_2O, and the intermediates OH and CHO. Although no other species containing nitrogen were predicted to exist at this location, namely N and NO, the mass fraction of N_2 is at a minimum inside the plume core because of the presence of other major species such as H_2O, CHO and especially unburned CH_4.

Table 8.3: Maximum Mass Fraction for Various Species at 49.6 d_{eq}

Specie	Maximum Mass Fraction
CH_4	$8.05x10^{-2}$
CH_3	$1.09x10^{-8}$
H_2	$5.07x10^{-7}$
CHO	$1.45x10^{-5}$
H_2O	$8.48x10^{-6}$
OH	$4.32x10^{-20}$
N_2	$7.80x10^{-1}$
O_2	$2.20x10^{-1}$

8.3.1: Sources for Error

As with most CFD, calculations often do not exactly match the experimental results and must be "adjusted" to fit the data well. However, in this case, several straightforward improvements can be made. The first improvement should take into account the actual freestream total temperature of the wind tunnel, which is 280 K, rather than the 298 K that was assumed. The second lies within the turbulence model. Switching to the well-known k-ε model should provide more realistic results than the Baldwin-Lomax model, which was chosen based on its much faster computation time. This switch is expected to improve both the mixing trends of the CFD calculations and the temperature distribution near the floor of the tunnel. Another avenue of improvement may lie in trying a different combustion model, although other choices should be explored since increasing the number of species within the combustion model greatly increases computation time and may not necessarily improve the results. In addition, the total temperature rise predicted by the CFD, and experimentally observed in Chapter 6, had little to due with heat release from combustion, but rather was associated with the thermal energy initially imparted to the feedstock gas by the arc. Perhaps the area most open to consideration would be the assumptions made for the torch exit conditions and the energy absorbed by the gas. Clearly, the total temperature calculated by the CFD

code was lower than the actual, which may indicate that the assumption of 40% arc efficiency may be too low. This indicates that the bulk temperature used in the calculations would need to be increased, since it is directly related to the arc efficiency. The final area to investigate would be the grid itself. Changes should focus on increasing the density of grid points, or changing the geometry of the blocks to increase resolution in areas that are now known to be important. A combination of these suggestions should be easy to implement without greatly increasing the effort or computational time required, and would confirm whether these improvements were necessary. Based on these recommendations, Perrig (2001) performed a computational study comparing the k-ε and k-ω models in place of the Baldwin-Lomax, and a newly defined grid structure to better account for the penetration height of the plume. In addition, he also performed calculations with and without the Bowman-Seery reaction mechanism for methane to determine how the mechanism affected the results. He demonstrated that the use of the k-ε turbulence model greatly increased the accuracy of CFD calculations assuming non-reactive flow, whereas the k-ω model poorly predicted the shape of the plume. The k-ε results agree quite well with experimental observations, which indicate that the heat release due to combustion is minor compared to the initial thermal energy imparted by the arc. The implementation of the combustion mechanism using this model gave somewhat less accurate results, probably due to an incompatibility with other features of the CFD model. Further details of Perrig's work are shown in Appendix D.

8.4: Conclusions

CFD calculations were performed using GASP® to model a plasma torch operating with methane at 1500 watts and a momentum flux ratio of 1.17. Experiments performed in a Mach 2.4 crossflow under the same conditions were used to determine the accuracy of the model. Comparisons were made on the shock angles produced by the torch and downstream total temperature values.

It was found that the CFD calculations were in good agreement with some of the experimental measurements, namely the predictions of the bow shock angle and the penetration height of the downstream plume core. For the conditions specified, the bow shock angle was calculated to be 32° and the penetration height for the core of the

downstream plume was 3.25 d_{eq}. However, the CFD under predicted the maximum total temperature ratio of the plume core. The maximum total temperature ratio for the experimental results was 1.26, whereas for the CFD calculations it was 1.16. Underestimating the arc efficiency, rather than a deficiency in the model itself most likely caused this difference. In addition, the total temperature plot produced by the CFD code did not match well with the experimental results, both for plume shape and overall penetration characteristics. The total temperature plot produced from the experimental measurements showed that the plume is almost circular in nature and does not penetrate fully off the tunnel floor. However, the CFD calculations predicted the plume shape to be more elliptical and fully penetrated. The turbulence model is thought to be a possible source of this difference. Improvements to the CFD model by implementing the k-ε turbulence model and restructuring of the grid were made by Perrig (2001), for which the main results are shown in Appendix D.